NANO LETTERS

pubs.acs.org/NanoLett Letter

Can Copper Nanostructures Sustain High-Quality Plasmons?

Vahagn Mkhitaryan, Katia March, Eric Nestor Tseng, Xiaoyan Li, Leonardo Scarabelli, Luis M. Liz-Marzán, Shih-Yun Chen, Luiz H. G. Tizei, Odile Stéphan, Jenn-Ming Song, Mathieu Kociak,* F. Javier García de Abajo,* and Alexandre Gloter

Cite This: *Nano Lett.* 2021, 21, 2444–2452 Read Online

ACCESS | Metrics & More | Article Recommendations | Supporting Information

ABSTRACT: Silver, king among plasmonic materials, features low inelastic absorption in the visible-infrared (vis-IR) spectral region compared to other metals. In contrast, copper is commonly regarded as too lossy for actual applications. Here, we demonstrate vis-IR plasmons with quality factors >60 in long copper nanowires (NWs), as determined by electron energy-loss spectroscopy. We explain this result by noticing that most of the electromagnetic energy in these plasmons lies outside the metal, thus becoming less sensitive to inelastic absorption. Measurements for silver and copper NWs of different diameters allow us to elucidate the relative importance of radiative and nonradiative losses in plasmons spanning a wide spectral range down to <20 meV. Thermal population of such low-energy modes becomes significant and generates electron energy gains associated with plasmon absorption, rendering an experimental determination of the NW temperature. Copper is therefore emerging as an attractive, cheap, abundant material platform for high-quality plasmonics in elongated nanostructures.

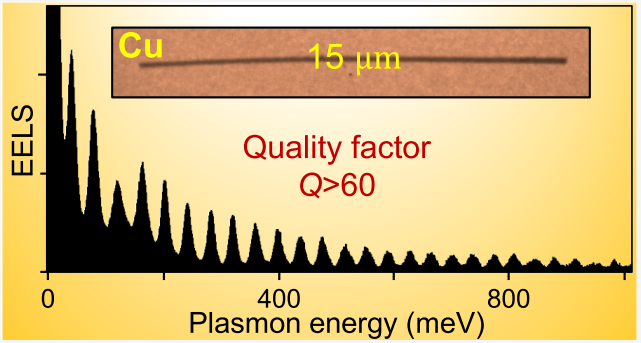

KEYWORDS: *high quality plasmons, copper plasmonics, nanowire plasmons, electron energy-loss spectroscopy (EELS), electron energy-gain spectroscopy (EEGS)*

Interest in plasmons has been largely fueled by the emergence and prospects of appealing applications, ranging from nonlinear[1−4] and quantum[5,6] optics to biosensing[7−10] and light harvesting.[11,12] While large inelastic absorption can be beneficial for a plasmonic approach to nanoscale thermal heating[13] and cancer therapy,[14] dissipation reduces the ability of plasmons to locally enhance the optical electromagnetic field, which is a unique property of these excitations and the ingredient that enables several of those applications. Low dissipation and high quality factor (i.e., the dimensionless product of frequency and lifetime, $Q = \omega\tau$) are thus desirable plasmon characteristics. Among metals, silver is widely identified as an excellent choice for this reason, as visible and IR plasmons in this material are less affected by quenching originating in the coupling to electron−hole-pair transitions, which lie at higher energies. However, the search for more abundant plasmonic materials continues. In particular, aluminum has been argued to operate in the ultraviolet regime thanks to its elevated bulk plasmon frequency and still relatively low level of losses.[15,16] In this context, gold and copper, which host a conduction electron density similar to silver, are considered to be inferior for IR plasmonics because their intrinsic lifetimes (∼9.3 and 6.9 fs, respectively) are ∼3 and 5 times shorter than that of silver (∼31 fs).[17] Still, gold is widely used because of its low reactivity and highly controlled growth,[18,19] while copper has been found to also produce well-defined plasmons in nanoplates[20] and CMOS waveguides.[21,22]

Characterization of plasmons is greatly facilitated by electron energy-loss spectroscopy (EELS), which allows us to map these excitations with nanometer spatial resolution.[23−25] Additionally, in contrast to far-field optical[26] and cathodoluminescence[27−29] techniques, EELS is sensitive to both bright and dark modes,[29,30] which is important to study plasmons that do not couple efficiently to propagating light. Visible[31,32] and IR[33] plasmons have been mapped using EELS with an increasing degree of spectral resolution, which is now pushed to the few millielectronvolts range by taking advantage of recent advances in electron microscopy instrumentation, making it possible to explore even mid-IR optical modes, such as those associated with atomic vibrations,[34−39] as well as low-energy plasmons and their interaction with phonon polaritons.[39]

Received: November 25, 2020
Revised: February 17, 2021
Published: March 2, 2021

https://dx.doi.org/10.1021/acs.nanolett.0c04667
Nano Lett. 2021, 21, 2444−2452

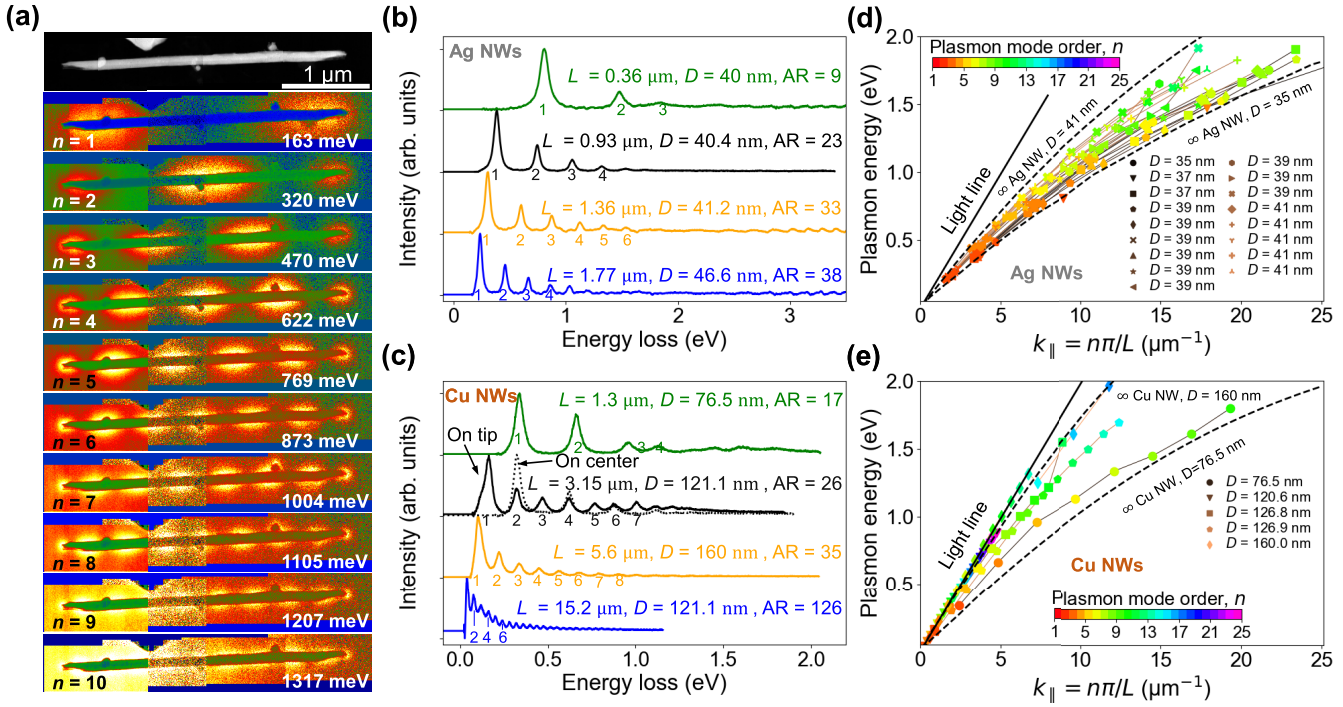

Figure 1. Infrared plasmons in long Ag and Cu NWs. (a) Plasmons of increasingly high infrared energy and order n sustained by a ~3.15 μm long Cu NW (see HAADF STEM image at the top) mapped through energy-filtered imaging. (b,c) Plasmonic EELS spectra collected near the tip of (b) Ag and (c) Cu NWs of varying geometrical parameters (length L, diameter D, and aspect ratio AR = L/D) after subtraction of the ZLP. A spectrum collected at the Cu NW center is shown in (c) (dashed curve), displaying only modes of even order n, compared with excitation of all values of n in the spectrum acquired near the tip of the same NW (black solid curve). (d,e) Dispersion relations obtained from (b,c) and additional similar spectra for (d) Ag and (e) Cu NWs. We consider different NW diameters D (see legends). Calculated dispersions of infinite NWs (dashed curves) are compared with data points (symbols). The latter are obtained by assigning a parallel wave vector $k_{\parallel} = n\pi/L$ depending on mode order n (see scales with symbol color) for each NW length L. NWs are deposited on a 15 nm thick Si_3N_4 substrate.

In this Letter, we show that elongated copper nanostructures can sustain spectrally sharp vis-IR plasmons of similar quality factor as in their silver counterparts. More precisely, we use high-resolution EELS to map and spectrally characterize plasmons in both copper and silver nanowires (NWs) with lengths ranging from hundreds of nanometers to >10 μm and displaying quality factors Q > 60. We present extensive measurements on both types of NWs that allow us to fully characterize the dependence of the plasmon spectral position and width on material and geometrical parameters. The mechanism that enables copper NWs to sustain high-quality plasmons relates to the fact that a large fraction of the electromagnetic energy resides outside the metal when the light wavelength is large compared with the wire diameter, thus reducing the effect of inelastic losses. We provide electromagnetic simulations in excellent agreement with our measurements, further revealing the effect of the substrate and the relative role of nonradiative and radiative losses. Interestingly, high-quality plasmons of sub-100 meV energy sustained by long copper NWs can also be revealed through the gain signatures that they imprint on the electron spectrum, as they are thermally populated at room temperature. These results support the use of elongated copper nanostructures for plasmonic applications requiring spectrally narrow, long-lived modes.

We start in Figure 1 with a comprehensive analysis of plasmons in Ag and Cu NWs for a wide range of geometrical parameters, resulting in mode energies that cover a range extending from ~20 meV to the onset of interband transitions in these metals. We base our analysis on state-of-the-art EELS with a combined energy and space resolution of ~10 meV and ~1 nm, respectively, as described in the Supporting Information (SI). Figure 1a shows energy-filtered EELS maps of a Cu NW of ~3.15 μm length (assembled from four separate maps of the NW), exhibiting a number of maxima given by n + 1, where n labels the order of the plasmon mode (i.e., this is the number of nodes in the plasmonic standing waves along the NW[24,32,40−44]). These characteristic standing waves have clear associated spectral signatures, as depicted in Figure 1b for Ag and in Figure 1c for Cu NWs (see Figure S1 for a comparison with calculated spectra). Both Ag and Cu spectra manifest the expected quasi-harmonic series of peaks, shifting to lower energy as the aspect ratio (AR = L/D) increases and following the dispersion relation defined for wires of infinite length, as represented in Figure 1d,e (see also Figure S2 for a selection of the data in Figure 1d that makes the comparison between different diameters clearer). However, closer and more quantitative analysis reveals major differences between both types of NWs. A first observation is an expected dependence of the dispersion relation on the wire diameter, with thinner NWs deviating more from the light line. Additionally, due to their longer lengths, Cu NWs display plasmons at lower energies. More strikingly, we clearly show that the dispersion relations for the Cu plasmons are much closer to the light line than those of silver NWs (i.e., Cu plasmons show a more retarded behavior than Ag plasmons); specifically, Cu NWs with lengths above 5 μm and diameters of the order of 160 nm permit reconstructing dispersion curves nearly indistinguishable from the light line up to plasmon energies of 1 eV. Deviations occur for shorter NW lengths or

https://dx.doi.org/10.1021/acs.nanolett.0c04667
Nano Lett. 2021, 21, 2444−2452

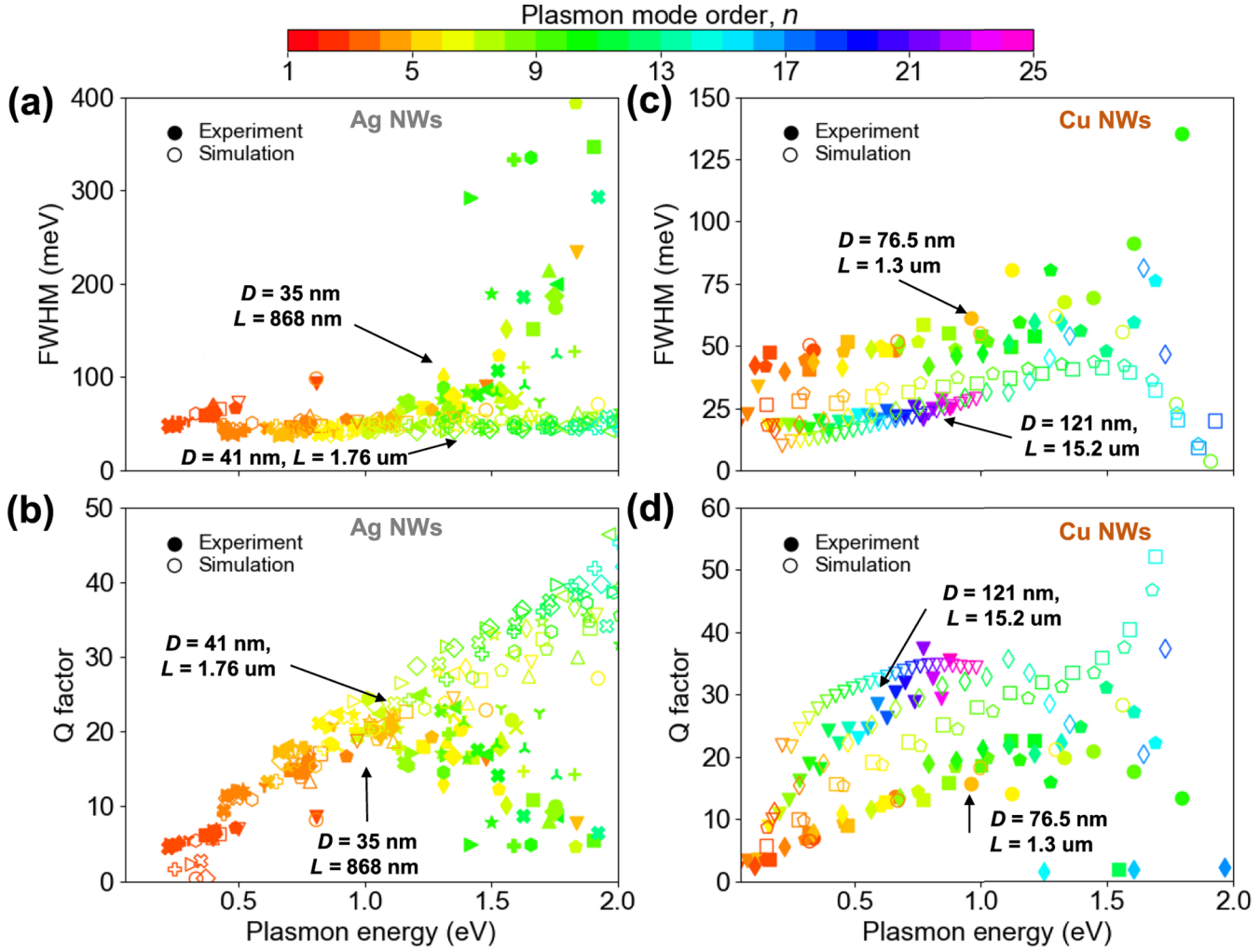

Figure 2. Plasmon width and quality factor. We show experimental (filled symbols) and simulated (open symbols) values of the fwhm (a,c) and quality factor Q (b,d) for Ag (a,b) and Cu (c,d) NWs collected over a broad range of geometrical parameters and mode order *n*. The experimental fwhm is obtained by Lorentzian fitting directly from the as-measured data (i.e., without deconvolution). NW diameters are encoded in the symbol types, which are the same as in Figure 1d,e, with maximum and minimum values as indicated by labels in each plot.

smaller diameters. Incidentally, in Figure 1e a series of plasmon modes with a substantial departure from the light line (in a behavior similar to Ag NWs) is observed for a Cu NW with a length of 1.3 μm and a relatively small diameter D = 76.5 nm.

We now move to the analysis of the plasmon spectral widths. Major differences between the two metals also occur in the behavior of the full-width at half-maximum (fwhm) and quality factor (see SI), which we plot as a function of plasmon energy for Cu and Ag NWs in Figure 2. For Ag NWs (Figure 2a,b), the experimentally observed fwhm's follow a monotonic increase from 40 to 400 meV as the plasmon energy is raised. At low energy, the fwhm's of dipolar modes (n = 1, red marks) display a very slow increase with energy. A similar behavior is encountered in other low-n modes. However, for each value of the plasmon energy, the fwhm decreases with mode order n in this regime. The fwhm's of plasmons at all orders continue to slowly increase with resonance energy until this approaches ~1.8 eV. Around this energy, the fwhm suddenly increases dramatically from less than 100 meV to values exceeding 400 meV. This behavior could be partially attributed to the presence of a ~200 nm Au nanorod seed used in the growth of Ag NWs.[44] Although this Au core is much smaller than the overall wire lengths under consideration, it is still capable of producing inelastic losses at the onset of interband transitions above ~1.5−2.5 eV in Au (compared with ~4 eV in Ag). This conclusion is consistent with numerical simulations performed with and without inclusion of the Au core (see Figure S9), where the former undergo a sudden increase in plasmon width above 2 eV. Still, the onset of losses in experiment occurs at a slightly lower energy, an effect that could originate in nonlocal effects associated with the small thickness of the Ag coating around the Au seed.

We find that the fwhm in the studied Cu NWs is systematically smaller than in Ag NWs. In Figure 2c, the measured fwhm of Cu NWs varies from 20 to 150 meV. As a general trend, the widths increase with plasmon energy, which is a behavior also observed in Ag NWs. Additionally, the minimum energy width is actually not found in the dipolar mode but often in multipolar modes at resonance energies of ~300 meV. We also analyze much longer (>15 μm) nanowires for which the fwhm is smaller than the instrumental spectral resolution. A near constant fwhm at low energies translates into a linear increase in quality factor Q with plasmon energy (Figure 2b,d). For Ag NWs (Figure 2b), the quality factors steadily increase from ~4 to ~25 and start decreasing above resonance energies around 1.3 eV. In Cu NWs (Figure 2d),

https://dx.doi.org/10.1021/acs.nanolett.0c04667
Nano Lett. 2021, 21, 2444−2452

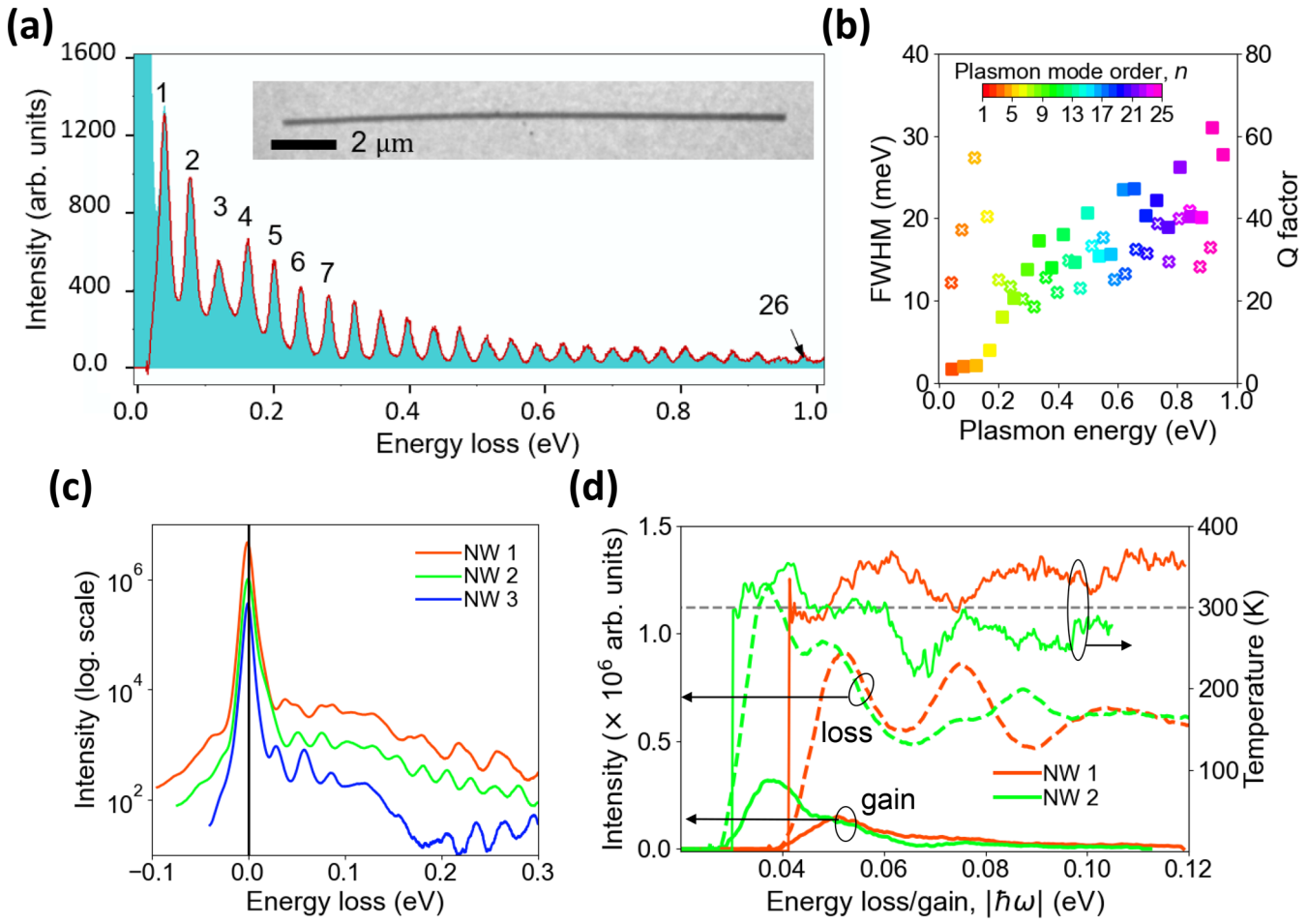

Figure 3. Electron-induced absorption and emission of infrared plasmons in a long Cu NW. (a) EELS spectrum measured at the tip of a long Cu NW (15.2 μm length, 121 nm diameter, see bright-field image in the inset). (b) fwhm (crosses, left scale) and quality factor Q (squares, right scale) obtained from the spectrum in (a). (c) EELS spectra revealing plasmonic energy gains associated with thermally excited IR plasmons (see features in the negative energy loss region), as probed with the electron beam focused near the tip of three long Cu NWs of length $L > 20$ μm. (d) Detail of the loss and gain inelastic electron intensities $I_{loss}(\omega)$ and $I_{gain}(\omega)$ (left scale) for NWs 1 and 2 (taken from (c) after elimination of the ZLP region), along with the temperature determined from $T = (\hbar\omega/k_B)/\log[I_{loss}(\omega)/I_{gain}(\omega)]$ (right scale). Data in panels a–c are deconvoluted, and the ZLP is subtracted from the cyan curve of (a). Data in panel (d) are not deconvoluted.

even larger quality factors are determined (e.g., $Q \sim 25$ and 35 in Ag and Cu NWs at 1 eV, respectively). These conclusions are consistent with the calculated plasmon propagation length $L_p = 1/2\ \mathrm{Im}\{k_p\}$ in infinitely long Ag and Cu NWs, as obtained from the complex plasmon wave vector k_p (see Figure S3, where we consider similar NW parameters as in Figure 1d,e).

As the NW length increases, low-order plasmons move toward increasingly smaller energies below those explored in Figures 1 and 2. The resulting spectra need to be deconvoluted from the zero-loss peak (ZLP) in order to increase the spectral resolution, which we bring from 14 to 8 meV by using the Richardson–Lucy algorithm[45] (see Section S2 and Figures S6 and S7 in Supporting Information). We present an example of this procedure in Figure 3a, showing a spectrum acquired near the tip of a long Cu NW (15.2 μm length, 121 nm diameter) and characterized by a long series of plasmon standing waves that reaches an order $n = 26$. A fwhm analysis of this spectrum (Figure 3b) reveals values down to 10 meV in plasmons of ~300 meV energy, whereas the quality factor exceeds $Q > 60$ at ~1 eV plasmon energy. Incidentally, the explored energy range includes phonon losses from the substrate, particularly at higher energies $\gtrsim$100 meV,[46,47] and we note that phonon–plasmon hybridization can reduce Q, as observed in silver NWs coupled to boron nitride phonons.[39]

We find it interesting that these long Cu NWs sustain well-defined plasmons at energies that are low enough to be thermally activated at room temperature (i.e., for $\hbar\omega \lesssim k_BT \sim$ 26 meV), as emphasized by the presence of energy gain peaks observed in the measured spectra of Figure 3c, thus extending the field of EELS thermometry from optical phonons[48,49] to mid-IR plasmons. Using very general arguments, we can write the inelastic electron probability for a sample in thermal equilibrium at temperature T as $\Gamma^T(\omega) = \Gamma(|\omega|)[n_T(\omega) + 1]\,\mathrm{sign}(\omega)$, where $\omega > 0$ ($\omega < 0$) refers to loss (gain) events, $\Gamma(|\omega|)$ is the EELS probability at zero temperature, and $n_T(\omega) = (e^{\hbar\omega/k_BT} - 1)^{-1}$ is the Bose–Einstein distribution function (see ref 50 for a tutorial derivation of this result). Consequently, the measured intensities of the loss and gain parts of the spectrum ($I_{loss}(\omega) \propto \Gamma^T(\omega)$ and $I_{gain}(\omega) \propto \Gamma^T(-\omega)$, taking ω as positive) are proportional to $n_T(\omega) + 1$ and $n_T(\omega)$, respectively, with the same proportionality function. This allows us to determine the sample temperature from the ratio of loss-to-gain peak intensities as $I_{loss}(\omega)/I_{gain}(\omega) = [n_T(\omega) + 1]/n_T(\omega) = e^{\hbar\omega/k_BT}$, which produces results

https://dx.doi.org/10.1021/acs.nanolett.0c04667
Nano Lett. 2021, 21, 2444–2452

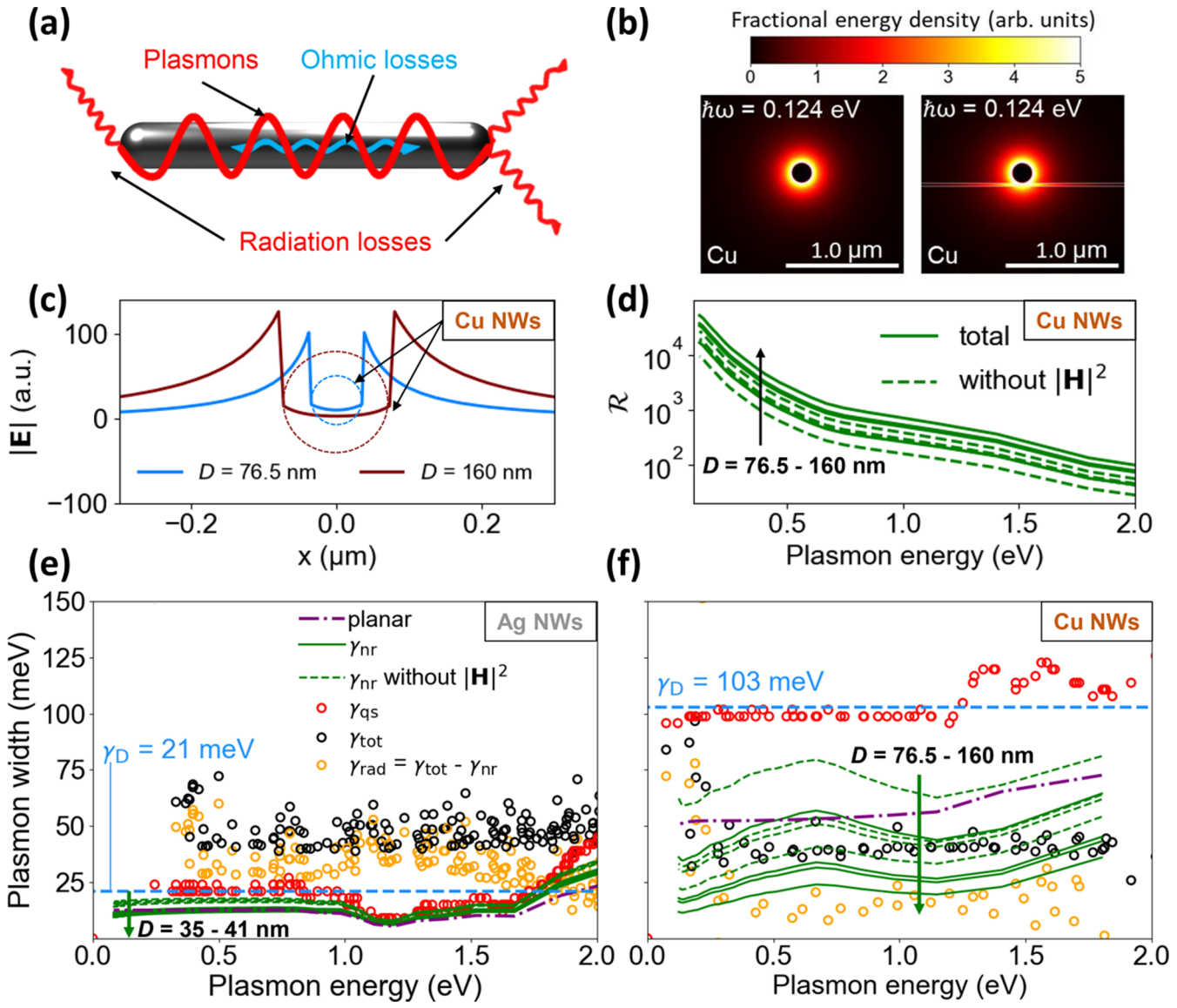

Figure 4. Radiative and nonradiative losses in the plasmons of Cu and Ag NWs. (a) Schematic representation of the loss mechanisms. (b) Calculated cross section of the electromagnetic energy density distribution in self-standing (left) and supported (right, 15 nm thick Si_3N_4 substrate) Cu NWs of 76.5 nm diameter and infinite length at 124 meV plasmon energy. (c) Radial distribution of the plasmonic electric near-field amplitude in self-standing infinite Cu NWs of diameters 76.5 and 160 nm (indicated by dashed circles) for 124 meV plasmon energy. (d) Ratio of the spatially integrated electromagnetic energy outside and inside self-standing Cu NWs of different diameters ($\mathcal{R}$, eq 2). Solid and dashed curves are calculated with and without inclusion of the magnetic field contribution. (e,f) Plasmon width contributions in (e) Ag and (f) Cu NWs: green curves represent the nonradiative rate γ_{nr} calculated from eq 1 with (solid curves) and without (broken curves) inclusion of the magnetic field for a range of increasing diameters D as indicated by the green arrows; black symbols show the total width γ_{tot} extracted from the fwhm simulations presented in Figure 2a,c for NWs within the same range of diameters and different lengths; orange symbols correspond to the radiative damping γ_{rad} estimated by subtracting γ_{nr} from the black circles; the Drude damping (blue) and the quasistatic damping (γ_{qs}, red) are shown for comparison. We also show results for the total decay rate of plasmons evolving in planar surfaces (purple dash-dotted curves).

around the temperature $T \sim 300$ K (with a substantial degree of instrumental error), as shown in Figure 3d, thus corroborating the thermal origin of the observed plasmon-related energy gain.

Further understanding of plasmons in Cu and Ag NWs can be gained by examining radiative and nonradiative loss mechanisms from a theoretical viewpoint. We first note that the observed plasmons display symmetric patterns along the transverse wire direction (see Figure 1a); in fact, they correspond to modes that are axially symmetric in self-standing structures, with a small deformation from axial symmetry being produced by the presence of a thin substrate (see Figure 4b). Chiral plasmons with an $e^{im\varphi}$ azimuthal dependence and $m \neq 0$ are also supported, but they emerge at higher energies and leave a comparatively weak trace on the transmitted electrons.[51] The dominant NW plasmons have $m = 0$ symmetry and can be understood as Fabry−Perot (FP) resonances in a cavity, whereby the round-trip propagation along the length L is accounted for by a phase $2k_{\parallel}L$, where $k_{\parallel}$ is the material-, diameter-, and frequency-dependent wave vector in an infinite wire (Figure 1d,e), while reflection at the ends can be described through a coefficient r. The FP condition that signals the existence of plasmons becomes $k_{\parallel}L + \arg\{r\} = n\pi$, where n is the mode order, which we use as a label in Figures

https://dx.doi.org/10.1021/acs.nanolett.0c04667
Nano Lett. 2021, 21, 2444−2452

1−3. The presence of antinodes at the NW ends indicates that the phase of the so-defined reflection coefficient is $\arg\{r\} \sim 0$ (therefore, we ascribe[40] $k_{\parallel} = n\pi/L$ in Figure 1d,e), as confirmed by the small phase extracted from experimental data for finite NWs by comparison with the dispersion relation of infinitely extended NWs (see Figure S10). In addition, the high quality factors observed from the EELS plasmon features reveal that they propagate multiple times along the NW length during their lifetimes, and therefore $|r| \lesssim 1$. With this perspective in mind, we can consider that the plasmon modes are bound to the NW during propagation, while scattering at the ends can result in out-coupling to radiation, as illustrated in Figure 4a.

The quality factors of plasmons in Ag and Cu structures depend on the contribution to the dissipation rate coming from both radiative and nonradiative mechanisms. In particular, the nonradiative contribution is given by the ratio of the absorption power to the electromagnetic energy $\gamma_{nr} = P_{abs}/W$. These quantities are in turn related to the monochromatic electric and magnetic field intensities at the mode frequency ω combined with the position- and frequency-dependent local permittivity $\epsilon(\mathbf{r},\omega)$ as[52]

$$P_{abs}(\omega) = \frac{\omega}{2\pi}\int d^3\mathbf{r}\,|\mathbf{E}(\mathbf{r},\omega)|^2\,\mathrm{Im}\{\epsilon(\mathbf{r},\omega)\}$$

$$W(\omega) = \frac{1}{4\pi}\int d^3\mathbf{r}\,[|\mathbf{E}(\mathbf{r},\omega)|^2\partial_\omega\,\mathrm{Re}\{\omega\epsilon(\mathbf{r},\omega)\} + |\mathbf{H}(\mathbf{r},\omega)|^2]$$

Neglecting absorption at the NW ends and treating the plasmon mode in the above FP model, we need to evaluate these expressions for the $m = 0$ guided mode of an infinite wire as a function plasmon frequency ω. We find a nonradiative contribution to the decay rate given by

$$\gamma_{nr} = \frac{P_{abs}}{W} = \frac{2\omega\,\mathrm{Im}\{\epsilon_m(\omega)\}}{\partial_\omega\,\mathrm{Re}\{\omega\epsilon_m(\omega)\} + \mathcal{R}(\omega)} \quad (1)$$

where

$$\mathcal{R}(\omega) = \frac{\int d^3\mathbf{r}\,|\mathbf{H}(\mathbf{r},\omega)|^2 + \int_{out} d^3\mathbf{r}\,\epsilon_h(\mathbf{r})|\mathbf{E}(\mathbf{r},\omega)|^2}{\int_{in} d^3\mathbf{r}\,|\mathbf{E}(\mathbf{r},\omega)|^2} \quad (2)$$

Here, the *in* and *out* integration domains refer to the volume inside and outside the metal, respectively, $\epsilon_m(\omega)$ is the metal permittivity, and the host permittivity is $\epsilon_h(\mathbf{r}) = 1$ for self-standing NWs, but it depends on position (inside or outside the substrate) for supported NWs.

In the quasistatic (qs) limit, which is valid for small structures compared to the light wavelength, the spectral line shape associated with the excitation of a plasmon of frequency ω_p reduces to[53] $\sim\mathrm{Im}\{1/[\epsilon_m(\omega) - \epsilon_m(\omega_p)]\}$ both in EELS and in the optical extinction. In this limit, ω_p depends on material and morphology but not on the size of the structure. Additionally, radiative losses vanish, so the total decay rate γ_{qs} is given by the fwhm of the above expression. Although we use experimental dielectric functions in all of our simulations, it is instructive to consider that for a Drude-like response $\epsilon_m(\omega) = \epsilon_b - \omega_{bulk}^2/\omega(\omega + i\gamma)$, which provides a good fit to the measured permittivity of Ag ($\epsilon_b = 4.0$, $\hbar\omega_{bulk} = 9.17$ eV, $\hbar\gamma = 21$ meV) and Cu ($\epsilon_b = 8.0$, $\hbar\omega_{bulk} = 8.88$ eV, $\hbar\gamma = 103$ meV) at frequency ω below their respective interband regions,[17,53] the quasistatic line shape becomes $\sim\mathrm{Im}\{1/[\omega_p^2 - \omega(\omega + i\gamma)]\}$ and the decay rate is $\gamma_{qs} \approx \gamma$ for large plasmon energy compared with the intrinsic damping rate, $\omega_p \gg \gamma$. Reassuringly, inspection of eq 1 further reveals $\gamma_{nr} \approx \gamma$ in the quasistatic Drude approximation.

Figure 4c shows the simulated field amplitude distribution across the diameter of self-standing Cu NWs with diameters $D = 76.5$ and 160 nm and infinite length, clearly revealing a larger weight outside the metal, and thus anticipating a reduction of nonradiative losses relative to the quasistatic limit. We corroborate this conclusion by examining the ratio $\mathcal{R}$ (eq 2) in Figure 4d, where we find $\mathcal{R} \gg 1$ (the effect is dramatic at low energy as a result of the larger delocalization of the field, see Figure 4b), although the outside contribution to the electromagnetic energy decreases with increasing plasmon frequency as the NW dispersion relation evolves away from the light cone (Figure 1d,e). Additionally, the presence of a substrate contributes to increase localization (Figure 4b), thus lowering $\mathcal{R}$ at low energy.

The results of this theoretical analysis are presented in Figure 4e,f for Ag and Cu NWs within the range of diameters and lengths experimentally explored in this work. We compare the total plasmon width γ_{tot} (black symbols, extracted from the calculations in Figure 2a,c) to the nonradiative (γ_{nr}, eq 1, green curves) and radiative ($\gamma_{rad} = \gamma_{tot} - \gamma_{nr}$, orange symbols) contributions. As a general conclusion, we find that Ag NWs show a total damping that is slightly larger than for Cu NWs, a result that we attribute to an increase in radiative losses in the former due to their smaller diameter; although nonradiative losses in Cu are higher (cf. blue curves and red symbols in Figure 4e,f), the larger diameter of the Cu NWs results in substantially smaller radiative damping. Additionally, the ratio $\mathcal{R}$ in eq 2 increases with diameter (see Figure 4d), thus contributing to reduce the nonradiative damping as well (eq 1). We note however that although $\mathcal{R}$ is higher at lower energies, $\epsilon_m(\omega)$ also increases in this limit (e.g., in the Drude limit, $\omega\,\mathrm{Im}\{\epsilon_m(\omega)\}$ and $\partial_\omega\,\mathrm{Re}\{\omega\epsilon_m(\omega)\}$ scale as $\gamma\omega_{bulk}^2/(\omega^2 + \gamma^2)$ and $\epsilon_b + \omega_{bulk}^2(\omega^2 - \gamma^2)/(\omega^2 + \gamma^2)^2$, respectively), so the overall dependence of γ_{nr} on frequency results from the interplay between these two quantities, and in fact, we observe in Figure 4e,f (green curves) a rather featureless nonradiative damping. We also note that γ_{rad} depends on how good the coupling to the far field is, which in turn is highly sensitive to NW geometry and mode order.[32] In particular, low-order modes have stronger coupling to the far field. Importantly, the presence of the Si_3N_4 substrate is found from theory to lower the quality factor of Ag NWs by ∼30% relative to self-standing NWs (see Figure S9). Incidentally, in much longer NWs (e.g., ∼100 μm in Figure S8) the spectral resolution of the microscope is not enough to discern low-energy plasmons close to the ZLP, but high-order modes can be identified with an energy spacing as low as 10−15 meV thanks to the achieved 8−10 meV EELS resolution.

In conclusion, by systematically investigating high-resolution EELS of micron-sized silver and copper NWs, we have unveiled high-quality vis-IR plasmons in both of these systems, thus challenging the commonly accepted view that copper is an inferior plasmonic material. We show that a substantial fraction of the electromagnetic energy associated with plasmons resides outside the metal, thus explaining the reduction in the relative effect of ohmic losses in these modes. We find that thicker nanowires bring the plasmons closer to the behavior of a planar surface, which for the energies under consideration (i.e., such that the metal has large absolute values of the permittivity) implies that the dispersion relation becomes closer to the light line (i.e., more photon-like) with a larger fraction of the

https://dx.doi.org/10.1021/acs.nanolett.0c04667
Nano Lett. 2021, 21, 2444−2452

plasmon energy placed outside the metal, thereby protecting these modes from the effect of ohmic losses. The interplay between radiative and nonradiative losses results in measured quality factors as high as $Q > 60$ in the near-IR part of the spectrum. Our measurements extend up to very low plasmon energies (<20 meV) in the mid-IR, where thermal population at room temperature is enough to produce traces in the energy gain side of the electron spectra. Indeed, we report a quantitative estimate of the NW temperature obtained from the ratio of loss-to-gain measured electron intensities in the mid-IR plasmonic region. The observed mechanism of loss reduction is promising for further applications of plasmons because it enables high quality modes even in intrinsically lossy materials such as Cu, which could offer additional functionalities related to their thermal, electrical, and thermoelectrical properties. Other cheap and abundant metals could be envisaged (see Figure S4), provided they can be grown in the form of long and thick structures, as shown here for copper nanowires.

■ ASSOCIATED CONTENT

Supporting Information

The Supporting Information is available free of charge at https://pubs.acs.org/doi/10.1021/acs.nanolett.0c04667.

Sections S1−S4: Details on NW synthesis and sample preparation, electron microscopy and EELS, electromagnetic simulations, deconvolution of EELS instrumental broadening, retrieval of plasmon full-width at half-maximum, and additional figures. Figure S1: Comparison between measured and calculated EELS spectra. Figure S2: Selection of results from Figure 1d. Figure S3: Plasmon dispersion and propagation length in infinitely long Ag and Cu NWs of selected diameters. Figure S4: Plasmon propagation in representative planar metal surfaces. Figure S5: Composition and crystallography of Cu NWs. Figures S6−S8: Details of plasmon width determination. Figure S9: Finite-difference time-domain simulations of the spectral width and quality factor Q of Cu and Ag NWs. Figure S10: Phase of the plasmon reflection coefficient r at the ends of Cu and Ag NWs (PDF)

■ AUTHOR INFORMATION

Corresponding Authors

Mathieu Kociak − *Laboratoire de Physique des Solides, Université Paris-Saclay, CNRS, 91405 Orsay, France;* orcid.org/0000-0001-8858-0449; Email: mathieu.kociak@universite-paris-saclay.fr

F. Javier García de Abajo − *ICFO-Institut de Ciencies Fotoniques, The Barcelona Institute of Science and Technology, 08860 Castelldefels, Spain; ICREA-Institució Catalana de Recerca i Estudis Avançats, 08010 Barcelona, Spain;* orcid.org/0000-0002-4970-4565; Email: javier.garciadeabajo@nanophotonics.es

Authors

Vahagn Mkhitaryan − *ICFO-Institut de Ciencies Fotoniques, The Barcelona Institute of Science and Technology, 08860 Castelldefels, Spain*

Katia March − *Laboratoire de Physique des Solides, Université Paris-Saclay, CNRS, 91405 Orsay, France*

Eric Nestor Tseng − *Department of Materials Science and Engineering, National Taiwan University of Science and Technology, Taipei 106, Taiwan*

Xiaoyan Li − *Laboratoire de Physique des Solides, Université Paris-Saclay, CNRS, 91405 Orsay, France*

Leonardo Scarabelli − *CIC biomaGUNE, Basque Research and Technology Alliance (BRTA), 20014 Donostia-San Sebastián, Spain*

Luis M. Liz-Marzán − *CIC biomaGUNE, Basque Research and Technology Alliance (BRTA), 20014 Donostia-San Sebastián, Spain; Ikerbasque, Basque Foundation for Science, 38013 Bilbao, Spain; Centro de Investigación Biomédica en Red, Bioingeniería, Biomateriales y Nanomedicina (CIBER-BBN), 28014 Donostia-San Sebastián, Spain;* orcid.org/0000-0002-6647-1353

Shih-Yun Chen − *Department of Materials Science and Engineering, National Taiwan University of Science and Technology, Taipei 106, Taiwan*

Luiz H. G. Tizei − *Laboratoire de Physique des Solides, Université Paris-Saclay, CNRS, 91405 Orsay, France;* orcid.org/0000-0003-3998-9912

Odile Stéphan − *Laboratoire de Physique des Solides, Université Paris-Saclay, CNRS, 91405 Orsay, France*

Jenn-Ming Song − *Department of Materials Science and Engineering, National Chung Hsing University, Taichung 402, Taiwan*

Alexandre Gloter − *Laboratoire de Physique des Solides, Université Paris-Saclay, CNRS, 91405 Orsay, France*

Complete contact information is available at: https://pubs.acs.org/10.1021/acs.nanolett.0c04667

Notes

The authors declare no competing financial interest.

■ ACKNOWLEDGMENTS

We acknowledge the use of (S)TEM at the John M. Cowley Center for High Resolution Electron Microscopy in the Eyring Materials Center at Arizona State University. This work has been supported in part by the National Agency for Research under the program of future investment TEMPOS CHROMATEM (ref. no. ANR-10-EQPX-50), the European Commission (Grants 823717 ESTEEM3, 101017720 FET-Proactive EBEAM, and FET-Open 964591-SMART-electron), the European Research Council (Advanced Grant 789104-eNANO), the 2017-2018 France-Taiwan Orchid Program (ref. no. 106-2911-I-005-501), the Spanish MINECO (MAT2017-88492-R, MAT2017-86659-R, and SEV2015-0522), the Catalan CERCA Program, and Fundacións Cellex and Mir-Puig. L.S. acknowledges support from the Marie Skłodowska-Curie Action SHINE (H2020-MSCA-IF-2019, Grant 894847).

■ REFERENCES

(1) Palomba, S.; Danckwerts, M.; Novotny, L. Nonlinear Plasmonics with Gold Nanoparticle Antennas. *J. Opt. A: Pure Appl. Opt.* **2009**, *11*, 114030.

(2) Kauranen, M.; Zayats, A. V. Nonlinear Plasmonics. *Nat. Photonics* **2012**, *6*, 737−748.

(3) Smirnova, D.; Kivshar, Y. S. Multipolar Nonlinear Nanophotonics. *Optica* **2016**, *3*, 1241−1255.

(4) Jain, P. K.; Huang, X. H.; El-Sayed, I. H.; El-Sayed, M. A. Noble Metals on the Nanoscale: Optical and Photothermal Properties and Some Applications in Imaging, Sensing, Biology, and Medicine. *Acc. Chem. Res.* **2008**, *41*, 1578−1586.

(5) Chang, D. E.; Sörensen, A. S.; Hemmer, P. R.; Lukin, M. D. Quantum Optics with Surface Plasmons. *Phys. Rev. Lett.* **2006**, *97*, No. 053002.
(6) Fakonas, J. S.; Lee, H.; Kelaita, Y. A.; Atwater, H. A. Two-Plasmon Quantum Interference. *Nat. Photonics* **2014**, *8*, 317−320.
(7) Liedberg, B.; Nylander, C.; Lunström, I. Surface Plasmon Resonance for Gas Detection and Biosensing. *Sens. Actuators* **1983**, *4*, 299−304.
(8) Willets, K. A.; van Duyne, R. P. Localized Surface Plasmon Resonance Spectroscopy and Sensing. *Annu. Rev. Phys. Chem.* **2007**, *58*, 267−297.
(9) Kabashin, A.; Evans, P.; Pastkovsky, S.; Hendren, W.; Wurtz, G.; Atkinson, R.; Pollard, R.; Podolskiy, V.; Zayats, A. Plasmonic Nanorod Metamaterials for Biosensing. *Nat. Mater.* **2009**, *8*, 867−871.
(10) Zeng, S.; Baillargeat, D.; Ho, H.-P.; Yong, K.-T. Nanomaterials Enhanced Surface Plasmon Resonance for Biological and Chemical Sensing Applications. *Chem. Soc. Rev.* **2014**, *43*, 3426−3452.
(11) Atwater, H. A.; Polman, A. Plasmonics for Improved Photovoltaic Devices. *Nat. Mater.* **2010**, *9*, 205−213.
(12) Clavero, C. Plasmon-Induced Hot-Electron Generation at Nanoparticle/Metal-Oxide Interfaces for Photovoltaic and Photocatalytic Devices. *Nat. Photonics* **2014**, *8*, 95−103.
(13) Baffou, G. *Thermoplasmonics: Heating Metal Nanoparticles Using Light*; Cambridge University Press: Cambridge, 2017.
(14) O'Neal, D. P.; Hirsch, L. R.; Halas, N. J.; Payne, J. D.; West, J. L. Photo-Thermal Tumor Ablation in Mice Using Near Infrared-Absorbing Nanoparticles. *Cancer Lett.* **2004**, *209*, 171−176.
(15) Sanz, J. M.; Ortiz, D.; Alcaraz de la Osa, R.; Saiz, J. M.; Gonzalez, F.; Brown, A. S.; Losurdo, M.; Everitt, H. O.; Moreno, F. UV Plasmonic Behavior of Various Metal Nanoparticles in the Near- and Far-Field Regimes: Geometry and Substrate Effects. *J. Phys. Chem. C* **2013**, *117*, 19606−19615.
(16) Gerard, D.; Gray, S. K. Aluminium Plasmonics. *J. Phys. D: Appl. Phys.* **2015**, *48*, 184001.
(17) Johnson, P. B.; Christy, R. W. Optical Constants of the Noble Metals. *Phys. Rev. B* **1972**, *6*, 4370−4379.
(18) Grzelczak, M.; Pérez-Juste, J.; Mulvaney, P.; Liz-Marzán, L. M. Shape Control in Gold Nanoparticle Synthesis. *Chem. Soc. Rev.* **2008**, *37*, 1783−1791.
(19) Myroshnychenko, V.; Rodríguez-Fernández, J.; Pastoriza-Santos, I.; Funston, A. M.; Novo, C.; Mulvaney, P.; Liz-Marzán, L. M.; García de Abajo, F. J. Modelling the Optical Response of Gold Nanoparticles. *Chem. Soc. Rev.* **2008**, *37*, 1792−1805.
(20) Pastoriza-Santos, I.; Sánchez-Iglesias, A.; Rodríguez-González, B.; Liz-Marzán, L. M. Aerobic Synthesis of Cu Nanoplates with Intense Plasmon Resonances. *Small* **2009**, *5*, 440−443.
(21) Fedyanin, D. Y.; Yakubovsky, D. I.; Kirtaev, R. V.; Volkov, V. S. Ultralow-Loss CMOS Copper Plasmonic Waveguides. *Nano Lett.* **2016**, *16*, 362−366.
(22) Stebunov, Y. V.; Yakubovsky, D. I.; Fedyanin, D. Y.; Arsenin, A. V.; Volkov, V. S. Superior Sensitivity of Copper-Based Plasmonic Biosensors. *Langmuir* **2018**, *34*, 4681−4687.
(23) García de Abajo, F. J. Optical Excitations in Electron Microscopy. *Rev. Mod. Phys.* **2010**, *82*, 209−275.
(24) Kociak, M.; Stéphan, O. Mapping Plasmons at the Nanometer Scale in an Electron Microscope. *Chem. Soc. Rev.* **2014**, *43*, 3865−3883.
(25) Polman, A.; Kociak, M.; García de Abajo, F. J. Electron-Beam Spectroscopy for Nanophotonics. *Nat. Mater.* **2019**, *18*, 1158−1171.
(26) Zhang, S.; Bao, K.; Halas, N. J.; Xu, H.; Nordlander, P. Substrate-Induced Fano Resonances of a Plasmonic Nanocube: A Route to Increased-Sensitivity Localized Surface Plasmon Resonance Sensors Revealed. *Nano Lett.* **2011**, *11*, 1657−1663.
(27) Yamamoto, N.; Araya, K.; García de Abajo, F. J. Photon Emission from Silver Particles Induced by a High-Energy Electron Beam. *Phys. Rev. B: Condens. Matter Mater. Phys.* **2001**, *64*, 205419.
(28) Vesseur, E. J. R.; de Waele, R.; Kuttge, M.; Polman, A. Direct Observation of Plasmonic Modes in Au Nanowires Using High-Resolution Cathodoluminescence Spectroscopy. *Nano Lett.* **2007**, *7*, 2843−2846.
(29) Losquin, A.; Zagonel, L. F.; Myroshnychenko, V.; Rodriguez-Gonzalez, B.; Tence, M.; Scarabelli, L.; Forstner, J.; Liz-Marzan, L. M.; Garcia de Abajo, F. J.; Stephan, O.; Kociak, M. Unveiling Nanometer Scale Extinction and Scattering Phenomena Through Combined Electron Energy Loss Spectroscopy and Cathodoluminescence Measurements. *Nano Lett.* **2015**, *15*, 1229−1237.
(30) Chu, M. W.; Myroshnychenko, V.; Chen, C. H.; Deng, J. P.; Mou, C. Y.; García de Abajo, F. J. Probing Bright and Dark Surface-Plasmon Modes in Individual and Coupled Noble Metal Nanoparticles Using an Electron Beam. *Nano Lett.* **2009**, *9*, 399−404.
(31) Bosman, M.; Ye, E.; Tan, S. F.; Nijhuis, C. A.; Yang, J. K. W.; Marty, R.; Mlayah, A.; Arbouet, A.; Girard, C.; Han, M. Y. Surface Plasmon Damping Quantified with an Electron Nanoprobe. *Sci. Rep.* **2013**, *3*, 1−7.
(32) Martin, J.; Kociak, M.; Mahfoud, Z.; Proust, J.; Gérard, D.; Plain, J. High-Resolution Imaging and Spectroscopy of Multipolar Plasmonic Resonances in Aluminum Nanoantennas. *Nano Lett.* **2014**, *14*, 5517−5523.
(33) Rossouw, D.; Botton, G. A. Plasmonic Response of Bent Silver Nanowires for Nanophotonic Subwavelength Waveguiding. *Phys. Rev. Lett.* **2013**, *110*, No. 066801.
(34) Krivanek, O. L.; Lovejoy, T. C.; Dellby, N.; Aoki, T.; Carpenter, R. W.; Rez, P.; Soignard, E.; Zhu, J.; Batson, P. E.; Lagos, M. J.; Egerton, R. F.; Crozier, P. A. Vibrational Spectroscopy in the Electron Microscope. *Nature* **2014**, *514*, 209−214.
(35) Lagos, M. J.; Trügler, A.; Hohenester, U.; Batson, P. E. Mapping Vibrational Surface and Bulk Modes in a Single Nanocube. *Nature* **2017**, *543*, 529−532.
(36) Hage, F. S.; Nicholls, R. J.; Yates, J. R.; McCulloch, D. G.; Lovejoy, T. C.; Dellby, N.; Krivanek, O. L.; Refson, K.; Ramasse, Q. M. Nanoscale Momentum-Resolved Vibrational Spectroscopy. *Sci. Adv.* **2018**, *4*, No. eaar7495.
(37) Hage, F. S.; Kepaptsoglou, D. M.; Ramasse, Q. M.; Allen, L. J. Phonon Spectroscopy at Atomic Resolution. *Phys. Rev. Lett.* **2019**, *122*, No. 016103.
(38) Hachtel, J. A.; Huang, J.; Popovs, I.; Jansone-Popova, S.; Keum, J. K.; Jakowski, J.; Lovejoy, T. C.; Dellby, N.; Krivanek, O. L.; Idrobo, J. C. Identification of Site-Specific Isotopic Labels by Vibrational Spectroscopy in the Electron Microscope. *Science* **2019**, *363*, 525−528.
(39) Tizei, L. H. G.; et al. Tailored Nanoscale Plasmon-Enhanced Vibrational Electron Spectroscopy. *Nano Lett.* **2020**, *20*, 2973−2979.
(40) Novotny, L. Effective Wavelength Scaling for Optical Antennas. *Phys. Rev. Lett.* **2007**, *98*, 266802.
(41) Rossouw, D.; Couillard, M.; Vickery, J.; Kumacheva, E.; Botton, G. A. Multipolar Plasmonic Resonances in Silver Nanowire Antennas Imaged with a Subnanometer Electron Probe. *Nano Lett.* **2011**, *11*, 1499−1504.
(42) Nicoletti, O.; Wubs, M.; Mortensen, N. A.; Sigle, W.; van Aken, P. A.; Midgley, P. A. Surface Plasmon Modes of a Single Silver Nanorod: An Electron Energy Loss Study. *Opt. Express* **2011**, *19*, 15371−15379.
(43) Peng, L.; Mortensen, N. A. Plasmonic-Cavity Model for Radiating Nano-Rod Antennas. *Sci. Rep.* **2015**, *4*, 3825.
(44) Mayer, M.; Scarabelli, L.; March, K.; Altantzis, T.; Tebbe, M.; Kociak, M.; Bals, S.; García de Abajo, F. J.; Fery, A.; Liz-Marzán, L. M. Controlled Living Nanowire Growth: Precise Control over the Morphology and Optical Properties of AgAuAg Bimetallic Nanowires. *Nano Lett.* **2015**, *15*, 5427−5437.
(45) Gloter, A.; Douiri, A.; Tencé, M.; Colliex, C. Improving Energy Resolution of EELS Spectra: An Alternative to the Monochromator Solution. *Ultramicroscopy* **2003**, *96*, 385−400.
(46) Loong, C.-K. Phonon Densities of States and Related Thermodynamic Properties of High Temperature Ceramics. *J. Eur. Ceram. Soc.* **1999**, *19*, 2241−2247.

https://dx.doi.org/10.1021/acs.nanolett.0c04667
Nano Lett. 2021, 21, 2444−2452

(47) Kuwabara, A.; Matsunaga, K.; Tanaka, I. Lattice Dynamics and Thermodynamical Properties of Silicon Nitride Polymorphs. *Phys. Rev. B: Condens. Matter Mater. Phys.* **2008**, *78*, No. 064104.
(48) Lagos, M. J.; Batson, P. E. Thermometry with Subnanometer Resolution in the Electron Microscope Using the Principle of Detailed Balancing. *Nano Lett.* **2018**, *18*, 4556−4563.
(49) Idrobo, J. C.; Lupini, A. R.; Feng, T.; Unocic, R. R.; Walden, F. S.; Gardiner, D. S.; Lovejoy, T. C.; Dellby, N.; Pantelides, S. T.; Krivanek, O. L. Temperature Measurement by a Nanoscale Electron Probe Using Energy Gain and Loss Spectroscopy. *Phys. Rev. Lett.* **2018**, *120*, No. 095901.
(50) García de Abajo, F. J.; Di Giulio, V. Optical Excitations with Electron Beams: Challenges and Opportunities. *Photonics*2020, accepted.
(51) Gómez-Medina, R.; Yamamoto, N.; Nakano, M.; García de Abajo, F. J. Mapping Plasmons in Nanoantennas Via Cathodoluminescence. *New J. Phys.* **2008**, *10*, 105009.
(52) Jackson, J. D. *Classical Electrodynamics*; Wiley: New York, 1999.
(53) Yu, R.; Liz-Marzán, L. M.; García de Abajo, F. J. Universal Analytical Modeling of Plasmonic Nanoparticles. *Chem. Soc. Rev.* **2017**, *46*, 6710−6724.

https://dx.doi.org/10.1021/acs.nanolett.0c04667
Nano Lett. 2021, 21, 2444−2452